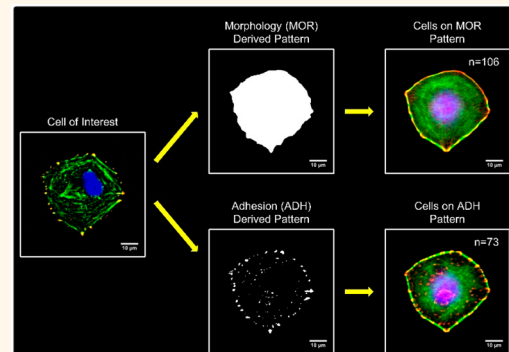


# Recapitulation and Modulation of the Cellular Architecture of a User-Chosen Cell of Interest Using Cell-Derived, Biomimetic Patterning

John H. Slater,<sup>†,‡</sup> James C. Culver,<sup>‡,||</sup> Byron L. Long,<sup>§</sup> Chenyue W. Hu,<sup>§</sup> Jingzhe Hu,<sup>§</sup> Taylor F. Birk,<sup>§</sup> Amina A. Qutub,<sup>§</sup> Mary E. Dickinson,<sup>‡</sup> and Jennifer L. West<sup>\*,†</sup>

<sup>†</sup>Department of Biomedical Engineering, Duke University, Durham, North Carolina, United States, <sup>‡</sup>Department of Molecular Physiology and Biophysics, Baylor College of Medicine, Houston, Texas, United States, and <sup>§</sup>Department of Bioengineering, Rice University, Houston, Texas, United States. <sup>||</sup>Present address: Department of Biomedical Engineering, University of Delaware, Newark, Delaware, USA (J.H.S.). <sup>||</sup>Present address: Cardiovascular Research Institute, University of California San Francisco School of Medicine, San Francisco, California, USA (J.C.C.).

**ABSTRACT** Heterogeneity of cell populations can confound population-averaged measurements and obscure important findings or foster inaccurate conclusions. The ability to generate a homogeneous cell population, at least with respect to a chosen trait, could significantly aid basic biological research and development of high-throughput assays. Accordingly, we developed a high-resolution, image-based patterning strategy to produce arrays of single-cell patterns derived from the morphology or adhesion site arrangement of user-chosen cells of interest (COIs). Cells cultured on both cell-derived patterns displayed a cellular architecture defined by their morphology, adhesive state, cytoskeletal organization, and nuclear properties that quantitatively recapitulated the COIs that defined the patterns. Furthermore, slight modifications to pattern design allowed for suppression of specific actin stress fibers and direct modulation of adhesion site dynamics. This approach to patterning provides a strategy to produce a more homogeneous cell population, decouple the influences of cytoskeletal structure, adhesion dynamics, and intracellular tension on mechanotransduction-mediated processes, and a platform for high-throughput cellular assays.



**KEYWORDS:** laser scanning lithography · image-guided patterning · biomimetic · cell-derived patterning · nanopatterning · self-assembled monolayers · actin cytoskeleton · cell adhesion · mechanotransduction · cell patterning · cell population heterogeneity · cell population homogeneity · cell engineering · cell arrays

High-throughput cellular assays are becoming increasingly important in drug screening, genomic profiling, and environmental impact studies. These assays are often implemented in an array format using high-resolution analysis techniques that allow for quantification of responses of individual cells or small cell populations to varied conditions.<sup>1,2</sup> Thus, intrinsic cellular heterogeneity has become increasingly problematic, as measurements may be confounded by subpopulations exhibiting highly varied responses.<sup>3–5</sup> Enrichment of cell populations with respect to expression of specific markers using techniques such as fluorescence-activated cell sorting (FACS) is often employed prior to

experimentation to minimize this problem.<sup>6</sup> In this study, we sought to provide an additional tool by gaining precise control over the morphology, adhesion site arrangement, and cytoskeletal architecture of cells to reduce population heterogeneity through mechanotransduction-mediated processes.<sup>7–9</sup> We developed an image-guided patterning strategy that utilized a user-chosen cell of interest (COI) as a template for laser-based, photothermal patterning of cell-derived configurations. We selected four COIs with varying morphologies and actin cytoskeletal architectures, derived two pattern configurations from each COI, one based on overall morphology that consisted of a single, continuous

\* Address correspondence to jennifer.l.west@duke.edu.

Received for review March 3, 2015 and accepted May 19, 2015.

Published online  
10.1021/acsnano.5b01366

© XXXX American Chemical Society

micropattern and the other on the COI's vinculin-containing adhesion sites that consisted of hundreds of discontinuous nano- to micrometer-sized patterns, fabricated arrays of both pattern types, and cultured cells on the arrays. We quantified the ability to recapitulate the COIs' architecture as defined by morphological, adhesion site, actin cytoskeletal, and nuclear properties in cells cultured on the corresponding biomimetic patterns. Applying a multimetric, image-based analysis interpreted by k-means clustering, we demonstrate that cells cultured on both cell-derived pattern configurations adopted an architecture that quantitatively resembled the original COI that the patterns were derived from, while nonpatterned control cells displayed widely varying architectures. Additionally, we demonstrate the ability to reproducibly prevent the formation of specific, user-chosen actin stress fibers using modified adhesion-derived pattern configurations and to significantly modulate adhesion site dynamics in cells displaying quantitatively similar architectures, providing a unique manipulation of mechanotransduction. This new approach to defining single-cell patterns and the ability to accurately pattern on the length scale of individual adhesion sites provides unprecedented control over cellular architecture, lays the foundation for inducing more homogeneous cell populations, and provides a potential array platform for high-throughput cellular assays.

## RESULTS AND DISCUSSION

**Image-Guided Laser Scanning Lithography.** To utilize images of a user-chosen COI as a template for surface patterning, we developed an image-guided, laser-based, photothermal patterning technique (Figure 1). The vinculin channel from an image of a COI (red in Figure 1a) was binarized and processed with custom-written MATLAB scripts to approximate the shape and arrangement of the COI's adhesion sites as a mosaic of quadrilaterals (Figure 1b,c).<sup>10</sup> The quadrilateral coordinates were exported as an overlay file written in a format utilized by Zeiss AIM software to define regions of interest (ROIs) for each shape within the mosaic (Figure 1c).<sup>10</sup> The ROIs (Figure 1c) defined patterns of a HS(CH<sub>2</sub>)<sub>11</sub>(OCH<sub>2</sub>CH<sub>2</sub>)<sub>6</sub>OH, oligo(ethylene glycol) (OEG), terminated self-assembled monolayer (SAM) (left panel in Figure 1e) that were thermally desorbed from a platinum (Pt)-coated glass coverslip by raster scanning a 532 nm laser focused through a 63× (NA 1.4) oil immersion objective operating at ~8.08 nJ/μm<sup>2</sup> in a nitrogen (N<sub>2</sub>)-rich atmosphere (middle panel in Figure 1e).<sup>11,12</sup> The patterned surfaces were exposed to fibronectin (FN) (right panel in Figure 1e), resulting in a pattern configuration (Figure 1d) that closely matched the adhesion site arrangement of the COI that the pattern was derived from (red in Figure 1a). This approach of using virtual masks, rather than physical masters required for many current patterning

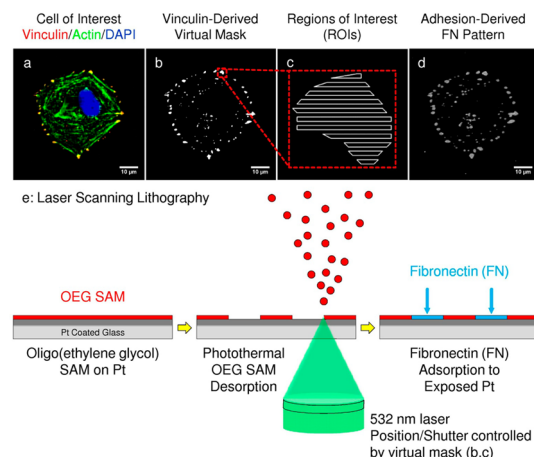


**Figure 1. Image-guided laser scanning lithography.** (a) The (red) vinculin channel from an image of a cell-of-interest (COI) was binarized and processed with custom-written MATLAB scripts to create a (b) virtual mask composed of (c) single pixel high quadrilaterals that act as regions of interest (ROIs) to control the laser position and shutter during (e) laser scanning lithography (LSL). (c) A zoomed in image of one adhesion site in the (b) virtual mask shows the single pixel high ROIs. (e) Schematic outlining the LSL process. A platinum (Pt)-coated glass coverslip was functionalized with an oligo(ethylene glycol) (OEG)-terminated alkanethiol. ROIs, as defined by the (c) quadrilaterals in the virtual mask, of the OEG self-assembled monolayer were thermally desorbed from the surface with a 532 nm laser focused through a 63× (NA 1.4) oil immersion objective. Fibronectin (FN) was adsorbed to the bare Pt patterns, resulting in an (d) image-derived FN pattern configuration that closely resembled (red in a) the cellular adhesion configuration that the pattern was derived from. (a, b, d) SB = 10 μm.

techniques, allowed for complex pattern configurations composed of nano- to micrometer-sized features to be fabricated rapidly, minimal restrictions on pattern-to-pattern spacing, and “on the fly” design modifications demonstrated in the following results.

**Characterization of Patterning Fidelity.** To evaluate the fidelity and reproducibility of image-guided laser scanning lithography (IG-LSL), arrays of the two FN pattern configurations derived from COI 1 (Figure 2b,f) were fabricated, the FN was fluorescently labeled, each pattern was imaged (see Supplemental Figures 1 and 2 for montages of the images used for analysis), the images were aligned and overlaid, and the average intensity was displayed as a heatmap (Figure 2d,h;  $n = 70$  and 103 for the number of images analyzed for the morphology- and adhesion-derived patterns, respectively). Overlays of the virtual masks (green in Figure 2e,i) and FN heatmaps (red in Figure 2e,i) were created to visually display the correlation between the COI and corresponding FN pattern features (yellow in Figure 2e,i).

To quantify the patterning fidelity, we analyzed the number (Figure 2k), size (Figure 2l), and shape (Figure 2m) of the pattern and COI features and implemented an Objects-Based correlation analysis (Figure 2j). The morphology-derived pattern consisted

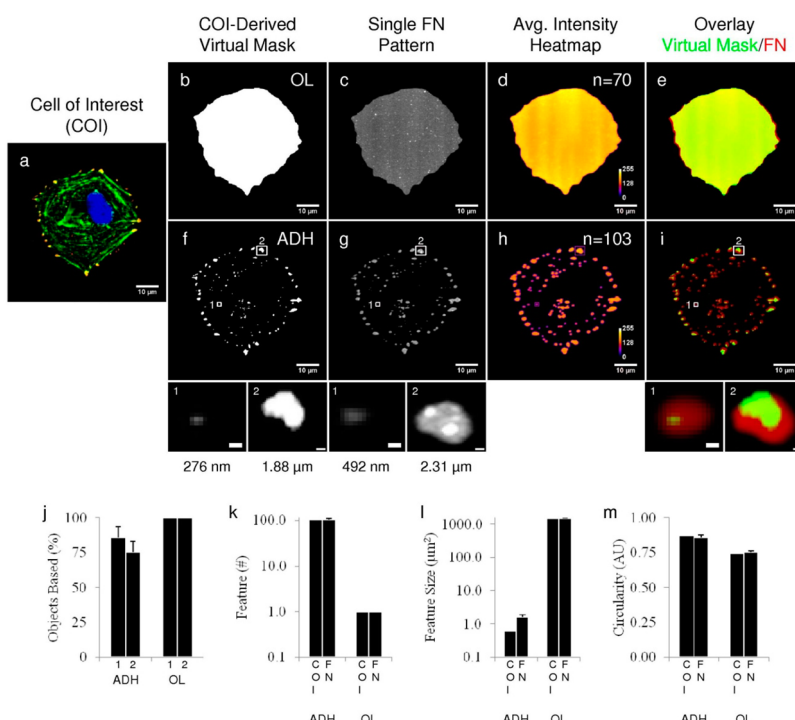


**Figure 2.** Analysis of patterning fidelity and reproducibility. (a) COI 1 was used to derive (b, f) two virtual masks; (b) one consisted of a single, continuous pattern derived from an outline (OL) of the COI and (f) the other a discontinuous pattern composed of 106 individual features derived from the COI's adhesion sites (ADH). (c, g) The size, orientation, and spatial organization of the features in FN pattern configurations closely matched the (a) COI that the patterns were derived from. (d, h) Multiple patterns were imaged, aligned, and overlaid to create average intensity heatmaps;  $n = 70$  and 103 for the number of images used for the morphology and adhesion site derived FN pattern configurations, respectively. (e, i) Overlays of the COI-derived (b, f; green) virtual masks and (d, h; red) heatmaps demonstrate a high level of correlation (yellow). An (j) Objects Based correlation analysis indicated a high degree of correlation between the FN patterns and COI. The (k) number, (l) size, and (m) shape of the features in the FN patterns closely matched the COI. The vertical bars indicate the measured values and are depicted as the mean  $\pm$  SD. (a–i) SB = 10  $\mu\text{m}$ . (Insets 1) SB = 300 nm. (Insets 2) SB = 500 nm.

of one continuous feature (Figure 2d,k) with an average size of  $1502 \pm 11 \mu\text{m}^2$  (Figure 2l) and circularity of  $0.757 \pm 0.006$  (Figure 2m) that closely matched the COI at  $1470 \mu\text{m}^2$  (Figure 2l) and 0.741 (Figure 2m), respectively, as indicated visually in the overlay (Figure 2e). One-hundred percent of the feature centroids between the outline of the COI and the morphology-derived patterns overlapped (Figure 2j, 1 indicates the % of the COI feature centroids that overlap with the FN pattern and vice versa for 2). Likewise, the adhesion-derived pattern configuration contained  $106 \pm 4$  (Figure 2k) features with an average circularity of  $0.855 \pm 0.022$  (Figure 2m) and size of  $1.582 \pm 0.316 \mu\text{m}^2$  (Figure 2l) that closely matched the number and shape of the COI's adhesion sites, 106 (Figure 2k) and 0.873 (Figure 2m), respectively, but were on average slightly larger than the COI's adhesion sites at  $0.604 \mu\text{m}^2$  (Figure 2l);  $86 \pm 8\%$  of the centroids of the COI's adhesions overlapped with the FN patterns, while  $76 \pm 7\%$  of the centroids of the FN patterns overlapped with the COI's adhesions (Figure 2j), indicating some spatial mismatch. A closer examination revealed that the smallest adhesion in the COI, with a characteristic length of  $\sim 276 \text{ nm}$  (inset 1 in Figure 2f), resulted in an FN pattern with a characteristic length of  $\sim 492 \text{ nm}$

(inset 1 in Figure 2g). At the resolution used for patterning, a single pixel had a width of 99 nm, indicating that the FN pattern was only 2–3 pixels larger than the adhesion used to define it. The extent of thermal spreading stayed the same ( $\sim 2\text{--}5$  pixels) regardless of the feature size and therefore had less of an influence on fidelity as pattern size increased. For example, a larger adhesion site in the COI (inset 2 in Figure 2f) with a characteristic length of  $1.88 \mu\text{m}$  was enlarged to only  $2.31 \mu\text{m}$  in the FN pattern (inset 2 in Figure 2g), a 1.5-fold increase in area.

Since LSL is a thermal-based process, feature enlargement occurs through in-plane lateral spreading of the heat generated in the metal film as the laser-induced surface plasmons decay.<sup>11–13</sup> This occurrence was minimized by utilizing low-conductivity thin Pt films, but even with this precaution very small features with a characteristic length less than  $\sim 300 \text{ nm}$  were slightly enlarged. The decrease in thermal conductivity provided by Pt allowed for lower energy patterning,  $8.08 \text{ nJ}/\mu\text{m}^2$  compared to  $33.38 \text{ nJ}/\mu\text{m}^2$  when using Au, which highly reduced patterning time to only  $\sim 17 \text{ ms}$  per pattern compared to  $\sim 1 \text{ s}$  for Au. These results demonstrate that a complex image containing hundreds of features over a broad range of sizes

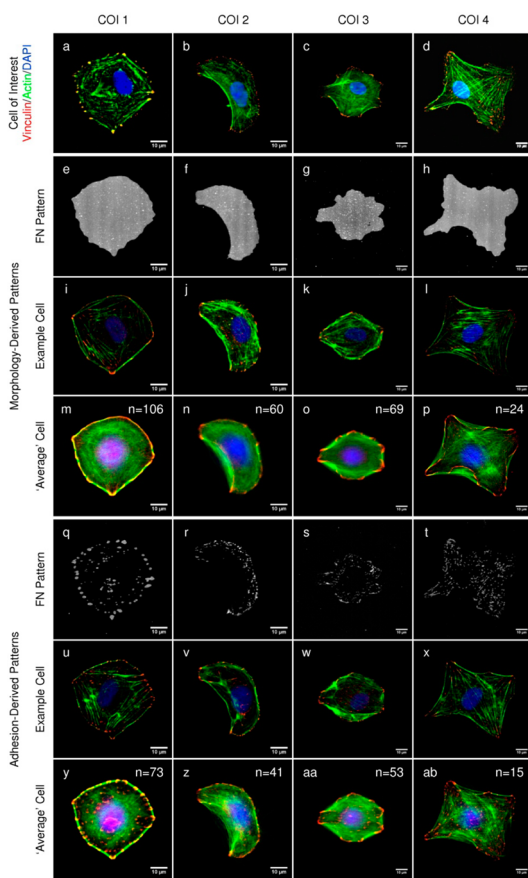


**Figure 3. Immunolabeled HUVECs cultured on cell-derived pattern configurations.** (a–d) Four cells of interest (COIs) were chosen from a population of HUVECs that were fixed, fluorescently immunolabeled for (red) vinculin and (green) actin, and (blue) counterstained with DAPI. Two pattern configurations were derived from each COI. (e–h) One configuration, derived from each COI's morphology, was composed of a continuous, cell-sized FN micropattern. (q–t) The other configuration, derived from an image of each COI's vinculin-containing adhesions (red in a–d), was composed of hundreds of individual, discontinuous FN nano- and micropatterns. Examples of immunolabeled HUVECs cultured on the (i–l) morphology- or (u–x) adhesion-derived pattern configurations. (m–p, y–ab) HUVECs cultured on pattern arrays were imaged, the images were aligned, and the intensity of each channel (vinculin, actin, DAPI) was averaged over all images (the number of imaged cells is indicated in the top right corner). The averaged channels were merged to create an “average” cell for each configuration. SB = 10  $\mu$ m.

and shapes could be accurately reproduced using IG-LSL.

**Development of Cell-Derived Pattern Configurations.** Human umbilical vein endothelial cells (HUVECs) were cultured on a FN-coated glass coverslip, fixed, and fluorescently stained for vinculin (red), actin (green), and nuclei (blue) (Figure 3a–d). Four COIs displaying varied cellular architectures were chosen and imaged (Figure 3a–d). COI 1 was chosen due to its cobblestone-like morphology typically observed in EC monolayers (Figure 3a), COI 2 due to its highly curved, keratocyte-like morphology typically not observed in ECs (Figure 3b), and COIs 3 and 4 (Figure 3c and 3d)

due to their extensive actin networks and intricate morphologies. Images of the four COIs were used to derive two pattern configurations from each COI: a morphology-derived pattern based on an outline (OL) of the COI (Figure 3e–h) and an adhesion site pattern (ADH) (Figure 3q–t) derived from an image of the vinculin-containing adhesions (red in Figure 3a–d, a in Supplemental Figure 3–6).

**Quantitative Analysis of the Degree of Recapitulation of a Cell-of-Interest's Architecture.** Arrays of the cell-derived pattern configurations (Figure 3e–h, q–t) were fabricated, and HUVECs were cultured on them for 16 h, fixed, stained for vinculin, actin, and nuclei, and imaged (Figure 3i–l, u–x). The cell images for each pattern configuration were aligned, overlaid, and intensity averaged to create “average” cell images representative of the population (Figure 3m–p, y–ab; see Supplemental Figures 3–6 for intensity averaged, overlaid images used to create the “average” cell-merged images).

An image-based, multimetric analysis was implemented to characterize the cellular architecture of each COI, patterned cell, and nonpatterned control cell, allowing quantification of the recapitulation of each COI's architecture using cell-derived patterns. Forty metrics were measured from the immunohistochemical images of each cell that encompassed 25 aspects of cellular architecture in four major categories: cell morphology, adhesion properties, actin cytoskeletal organization, and nuclear properties; see Supplemental Table 1 for details. Three-dimensional (3D) scatter plots displaying values for the four COIs (large colored data points), patterned cells (small colored data points), and nonpatterned controls (small black data points) are displayed in Figure 4a–c. The data points for the nonpatterned control cells were randomly dispersed throughout the scatter plots, indicating a large degree of heterogeneity in cellular architecture (Figure 4a–c). Conversely, cells cultured on the biomimetic patterns formed distinct clusters, as shown by the color groupings in the scatter plots, indicating a homogeneous cellular architecture (Figure 4a–c). Additionally, clustering of the COIs and cells cultured on corresponding patterns indicated that both pattern configurations, morphology- and adhesion-derived, induced a cellular architecture that closely resembled the COIs that the patterns were derived from (color-matched data points in Figure 4a–c).

Each COI and patterned cell was assigned a position in 40-dimensional space based on its measured metrics. The number of clusters present in the multidimensional data set was determined via a Silhouettes and stability gap analysis and indicated the presence of four distinct clusters. The cells belonging to each cluster were resolved using a k-means analysis with Euclidian distance as the similarity metric. Each of the four clusters was concentrated around each COI,

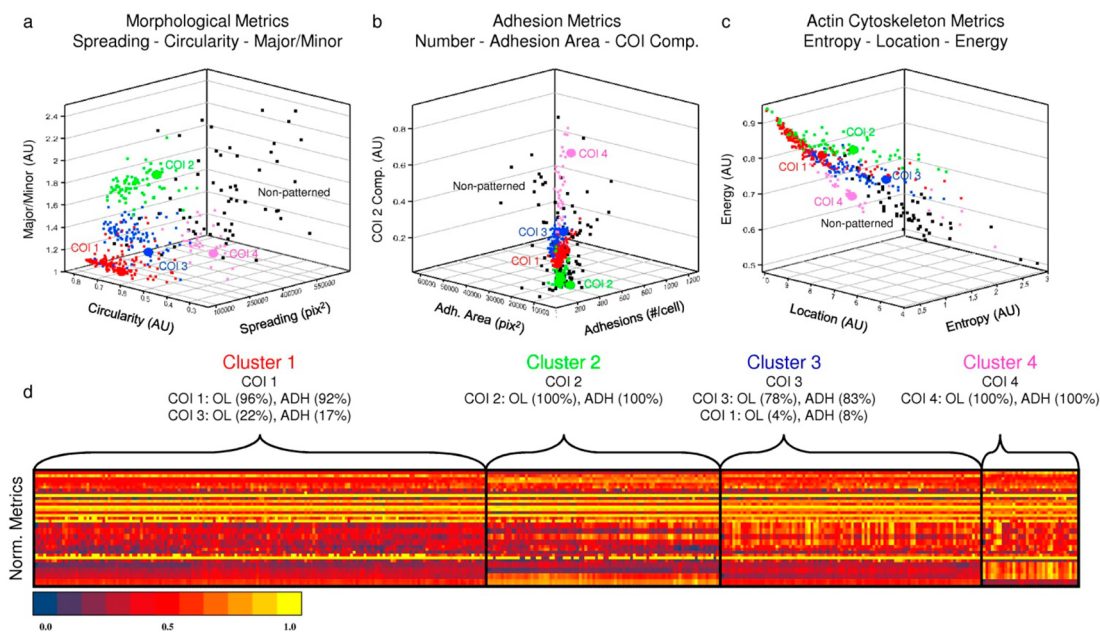


**Figure 4.** Cluster analysis to identify cells with similar architectures. (a–c) 3D scatter plots generated from three example metrics from three major categories used to characterize cellular architecture. The large spherical data points indicate measured values for the four COIs, the small colored data points indicate patterned cells and are color coded to indicate which COI the pattern was derived from, and the black data points indicate measured values for nonpatterned control cells. (d) Each patterned cell and COI was assigned a position in multidimensional space based on its 40 measured metric values. A silhouette and stability gap analysis indicated the presence of four distinct clusters/cellular architectures, and the cells belonging to each cluster were resolved using a k-means analysis. (d) The normalized metric values for each cell within each cluster are displayed as a heatmap. The cluster composition was determined by examining the percentage of the cell population from each pattern type that belonged to each cluster. Each cluster contains a COI (for example cluster 1 contains COI 1, cluster 2 COI 2, and so forth), and patterned cells whose architecture closely matched the COI in each cluster.

indicating that each COI possessed a quantitatively discernible and discrete cellular architecture that was recapitulated in the patterned cells. A heatmap displaying the normalized metric values for each COI and patterned cell and its cluster assignment was created to visually display the results (Figure 4d).

Analysis of the cells assigned to each cluster indicated that cell-derived pattern configurations were able to quantitatively induce recapitulation of the cellular architecture of the appropriate COI (Figure 4d). The cells that comprised clusters 2 and 4 displayed the best separation from cells on other pattern configurations. These clusters were comprised only of the COI used to define the pattern configurations and the cells cultured on the corresponding patterns (Figure 4d). For example, cluster 2 contained COI 2 and 100% of the population of cells cultured on both the morphology and adhesion configurations derived from COI 2 (Figure 4d). Cluster 4 displayed the same degree of recapitulation (Figure 4d). Clusters 1 and 3, defined by COIs 1 and 3, respectively, showed some crossover (Figure 4d). Cluster 1 contained COI 1, and 96% and 92% of the cell population cultured on the morphology and adhesion pattern configurations derived from COI 1, respectively (Figure 4d). Some cross-talk was observed where 22% and 17% of the cell population cultured on the morphology and adhesion patterns derived from COI 3, respectively, were present (Figure 4d). Similarly, cluster

3 contained COI 3 and 78% and 83% of the cell populations cultured on the morphology and adhesion configurations derived from COI 3, respectively (Figure 4d). Again some cross-talk was observed where 4% and 8% of the cell population cultured on the morphology and adhesion patterns derived from COI 1 appeared in cluster 3 (Figure 4d). The appearance of a small percentage of the cell population cultured on patterns derived from COI 1 in cluster 3 and vice versa indicated that some heterogeneity existed in the two cell populations, but the degree of population overlap was extremely small compared to the dispersion observed in nonpatterned control cells.

These results demonstrate that heterogeneity in cellular architecture can be highly reduced and that both cell-derived pattern configurations induced cells to adopt the architecture of the COI used to define the pattern configurations. The ability to recapitulate the characteristics of a user-chosen COI and to produce a more homogeneous cell population in a large array format using single-cell patterns potentially alleviates issues that arise from ensemble measurements of traditional, heterogeneous cell culture populations.

**Preventing the Formation of User-Chosen, Specific Actin Stress Fibers.** We quantitatively demonstrated that both pattern configurations recapitulated the cellular architecture of the appropriate COI. Here we demonstrate the ability to prevent the formation of user-chosen,

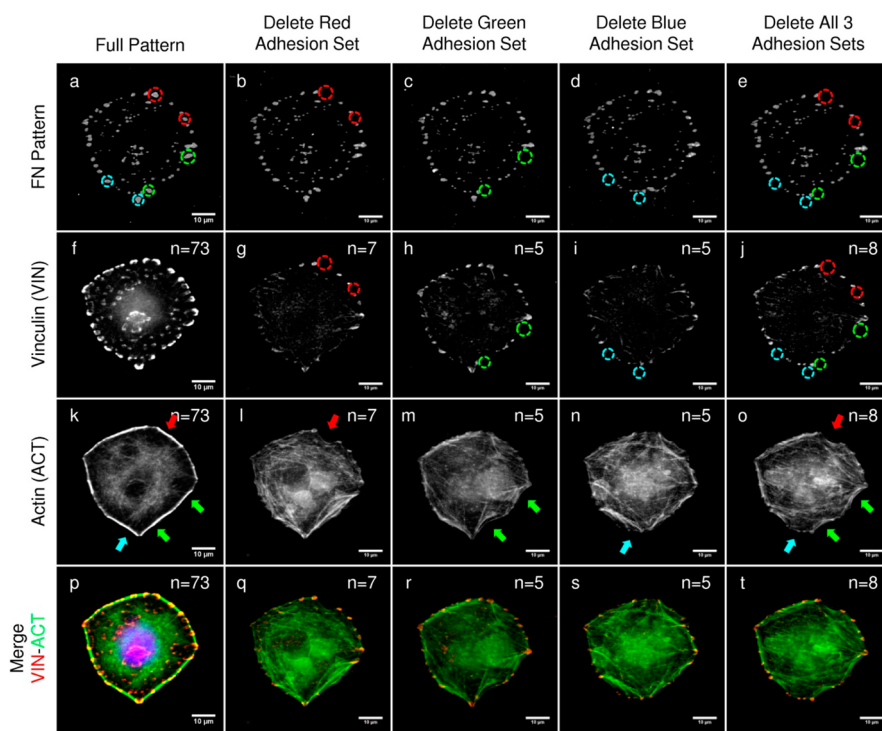


**Figure 5.** Preventing the formation of specific stress fibers using modified pattern configurations. (a) The adhesion site pattern configuration derived from COI 1 was modified so that specific pattern features that supported adhesions (matched color dashed circles in a) that anchored chosen actin stress fibers (arrows in k) were deleted from the configuration (b–e). (g–j) The formation of the chosen adhesion sites was suppressed with the modified pattern configurations and (l–o) therefore prevented the formation of the chosen stress fibers. SB = 10  $\mu$ m.

specific actin stress fibers using “on the fly” modifications to an adhesion-derived configuration. This ability to “delete” specific actin stress fibers and their anchoring adhesions provides an unprecedented level of control over cytoskeletal architecture and a systematic approach to investigate the influence of specific adhesion sites on mechanotransduction-mediated signaling processes. Figure 5a displays the full adhesion pattern derived from COI 1 and the corresponding adhesion sites (Figure 5f) and actin architecture (Figure 5k) of cells cultured on this pattern. We consistently observed the formation of stress fibers in specific locations along the cell periphery (colored arrows in Figure 5k), identified their corresponding anchoring adhesions (colored circles in Figure 5a), and tested the ability to prevent the formation of these stress fibers through simple pattern modifications.

In the first example the actin stress fiber indicated by the red arrow in Figure 5k was prevented from forming. The two individual patterns that supported the adhesion sites anchoring the red fiber were eliminated from the virtual mask, resulting in a pattern configuration lacking these two features (red circles in Figure 5b). Subsequently, cells cultured on this configuration did not form adhesions at these locations (red circles in Figure 5g) and therefore could not support a stress fiber (red arrow in Figure 5l), resulting in a “dip” in the actin cytoskeleton. This same approach

was implemented to selectively prevent the formation of two other stress fibers (blue and green arrows in Figure 5k, green arrows in Figure 5m, and blue arrow in Figure 5n). A pattern configuration void of all six features was implemented to simultaneously prevent the formation of all three stress fibers, resulting in a more dramatic alteration in actin architecture (Figure 5o). The chosen stress fibers were prevented from forming through simple “on the fly” modifications to the virtual mask used to define the pattern without the need to create new physical masters. This precise level of control opens new avenues for investigating mechanotransduction- and adhesion-mediated processes and provides a means to probe the contribution of specific adhesion sites on cell fate decisions.

**Manipulation of Adhesion Site Dynamics in Cells with Similar Architectures.** To independently probe the influences of intracellular force and dynamics on adhesion-mediated signaling, one must be able to induce cells to adopt similar cytoskeletal architectures while possessing the ability to modulate adhesion dynamics without chemical perturbation of the components that mediate signaling. Toward this goal we have demonstrated that both pattern configurations, morphology- and adhesion-derived, quantitatively induce a similar cellular architecture; however, we demonstrate that the adhesion site dynamics of cells on these two patterns are drastically different.

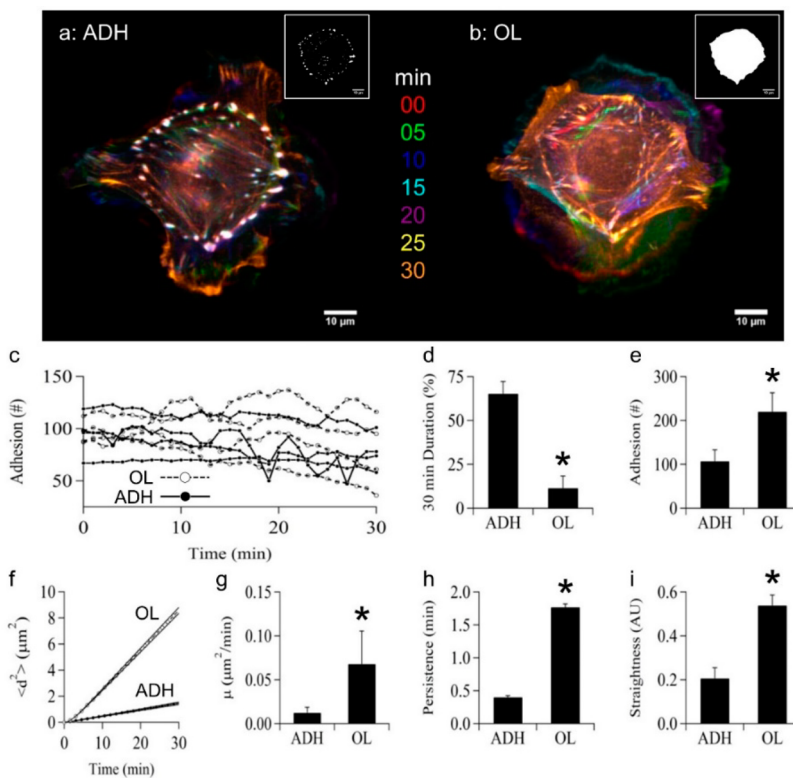


**Figure 6. Regulation of adhesion site dynamics.** GFP-talin-transduced HUVECs were cultured on (a) adhesion (ADH) or (b) morphology (OL) pattern configurations derived from COI 1, and their adhesion sites monitored at 1 min intervals for 30 min with time-lapse confocal microscopy. (a, b) False-colored images at 5 min intervals were overlaid; white features indicate static adhesion sites that maintained their position over the 30 min period. Insets in a and b indicate the pattern configuration. The time-lapse images were used to quantify the (c) number of adhesions present as a function of time, (d) percent of adhesions that persisted the 30 min period, (e) total number of adhesions formed over the 30 min period, (f) mean square displacement, and the (g) adhesion site mobility, (h) persistence, and (i) straightness. (a, b) SB = 10  $\mu\text{m}$ . \* indicates  $p < 0.05$ .

The influence of pattern type, morphology- (inset in Figure 6b) versus adhesion-derived (inset in Figure 6a), on adhesion site dynamics was investigated to determine whether defining adhesion placement and growth with a discontinuous, adhesion-derived pattern could be used to modulate the adhesive state of cells. HUVECs were transduced with GFP-talin, seeded on arrays of either the morphology (Figure 6b) or adhesion (Figure 6a) patterns derived from COI 1, given 4 h to adhere and spread, and imaged with time-lapse confocal microscopy at 1 min intervals for 30 min to track their adhesion sites. To visually display the differences in adhesion dynamics, images at 5 min intervals were false colored and summed to create a color-coded time map (Figure 6a,b). White regions indicate static adhesions that persisted over the entire 30 min, while adhesions that display only one or two colors persisted for only 5 or 10 min (Figure 6a,b). We observed that adhesions formed by cells cultured on the morphology-derived pattern were much more dynamic compared to cells on the adhesion-derived pattern (Figure 6, Supplemental Movies 1 and 2).

To quantify these observations, the adhesion sites were tracked and their properties quantified. Cells on both patterns possessed a similar number of adhesions

at any given time (Figure 6c); however,  $65 \pm 7\%$  (Figure 6d) of the adhesions formed by cells on the adhesion-derived pattern were maintained over the entire 30 min with an average lifetime of  $25.5 \pm 0.7$  min compared to only  $11 \pm 7\%$  (Figure 6d) with an average lifetime of  $12.5 \pm 2.3$  min for cells on the morphology-derived pattern ( $p = 0.00003$  for both the percent maintained and average lifetime). Even though cells on both pattern configurations possessed a similar number of adhesions at any given time, cells on the morphology-derived patterns formed over 2-fold more adhesions over 30 min,  $220 \pm 43$ , due to their increased turnover rate compared to only  $107 \pm 26$  (Figure 6e) for cells on the adhesion-derived pattern ( $p = 0.004$ ). For comparison, COI 1, from which the patterns were derived, exhibited 106 adhesions closely matching cells on the adhesion-derived pattern. Additionally, the extension and retraction of lamellipodia by cells on the morphology-derived pattern often led to sliding adhesions that were disassembled as new adhesions were formed in other regions of the cell (Supplemental Movie 1), similar to what has been observed at the trailing end of migrating cells.<sup>14</sup> These sliding adhesions induced a high degree of displacement that was not observed in cells on the adhesion-derived pattern

(Figure 6f, Supplemental Movie 2). The mobility coefficient (Figure 6g), analogous to a diffusion coefficient, and persistence time (Figure 6h) of the adhesion sites were measured from the mean square displacement (Figure 6f). Adhesions in cells on the adhesion-derived pattern had a mobility coefficient of only  $0.012 \pm 0.006 \mu\text{m}^2/\text{min}$  (Figure 6g) and a corresponding persistence time of  $0.400 \pm 0.030 \text{ min}$  (Figure 6h) compared to the significantly more dynamic adhesions in cells on the morphology-derived pattern that had a 5.67-fold higher mobility,  $0.068 \pm 0.038 \mu\text{m}^2/\text{min}$  (Figure 6g), and a 4.42-fold higher persistence time,  $1.770 \pm 0.050 \text{ min}$  (Figure 6h) ( $p = 0.028$  and  $0.034$  for the mobility coefficient and persistence time, respectively). The straightness of the adhesion site paths verified the existence of sliding adhesions in cells on the morphology-derived pattern with a measured value of  $0.54 \pm 0.05$  (Figure 6i) compared to only  $0.21 \pm 0.05$  (Figure 6i) for cells on the adhesion-derived pattern ( $p = 0.000\,007$ ).

This approach to patterning provides the ability to modulate adhesion site dynamics and to induce a more static user-chosen adhesive state that mimics the adhesion organization of a specific COI. While the exact role that adhesion dynamics plays in intracellular signaling events that dictate cell fate remains unknown, it is known that changes in adhesion dynamics are associated with a number of disease states.<sup>15</sup>

## CONCLUSIONS

Our approach of deriving pattern configurations from the overall morphology or adhesion site arrangement of a user-chosen cell rather than from simple geometric shapes provides a means to recapitulate the cellular architecture and potentially the tension state of a desired COI. The ability to induce increased population homogeneity with respect to a chosen COI's traits combined with the ability to create large arrays of cell-derived, single-cell patterns through automation provides a platform for high-throughput screening assays with potentially much lower variance in cell response compared to traditional cell culture approaches. While HUVECs were utilized as proof of principle, we anticipate that cell-derived patterning will prove useful for other adherent-dependent cell types, as all adherent-dependent cells utilize common mechanotransduction machinery. We envision applying this strategy to both fundamental cell studies and applications such as drug screening.

The ability to fine-tune cytoskeletal architecture, adhesion site dynamics, and the distribution of intracellular forces through simple "on the fly" pattern modifications provides an unprecedented level of control over cytoskeletal mechanics. It has been speculated that cytoskeletal tension-induced changes in cell behavior are transduced through cell adhesions.<sup>7</sup> Adhesions govern mechanotransduction-mediated

intracellular signaling events through their interaction with over 150 signaling components.<sup>16</sup> This has led to the idea that adhesion plaques act as mechanosensors that convert mechanical force into biochemical reactions, thereby acting as force-mediated regulators of intracellular signaling events.<sup>8</sup> Both adhesion site maturation, as indicated by adhesion site growth and changes in molecular composition through the sustained application of force,<sup>17–19</sup> and the dynamics of adhesion formation, maturation, and turnover influence mechanotransduction-mediated signaling events.<sup>15,19</sup> Accordingly, the implementation of surfaces presenting nano- to micrometer-sized patterns of an ECM component that allow for increased control over adhesion maturation and dynamics could provide a more controlled approach for modulating cell fate compared to regulation of cell spreading or shape.<sup>9</sup>

Signaling through adhesion sites has mostly been considered from a purely force-mediated perspective, in which changes in the molecular composition of adhesions during actomyosin-mediated maturation have been indicated as a key regulator of adhesion signaling.<sup>17–19</sup> Recent work suggests that adhesion site dynamics also plays an important role in adhesion-mediated signaling during embryonic development, immune cell function, and wound repair and cancer metastasis.<sup>15,19</sup> Modulation of adhesion site dynamics has been achieved via biochemical manipulation of adhesion site components<sup>20,21</sup> or motifs that govern adhesion dynamics<sup>22,23</sup> and has led to a wealth of knowledge of specific intracellular components that mediate adhesion turnover. The ability to manipulate adhesion dynamics using an outside-in approach provides an alternative, material-based means to probe the influence of adhesion dynamics without perturbation of the biochemical signaling motifs that govern adhesion dynamics. Along these lines, substrates with varying elasticity have been implemented to modulate adhesion dynamics<sup>24</sup> but inevitably also influence the cytoskeletal tension of cells.<sup>9</sup> While the importance of both force-mediated changes in the molecular composition of adhesions and the dynamics of this process have been indicated, there is no current system to simultaneously and independently investigate the influences of these processes; our approach overcomes this limitation.

Since the extent of cytoskeletal tension generated in cells is an important regulator of intracellular signaling cascades that mediate cell behavior<sup>7,25,26</sup> and since it has been speculated that this tension-mediated control likely emanates through changes in adhesion site signaling,<sup>7–9</sup> cell-derived, biomimetic patterning could potentially allow for the fabrication of surfaces displaying a large array of cells all behaving in a similar manner to the chosen COI used to define the patterns. This approach to recapitulating the architectural phenotype of a user-chosen COI opens a new avenue for

exploring mechanotransduction-mediated processes and their influence on cell fate. While the ability to modulate cell fate through regulation of cytoskeletal tension has provided much insight into the influence of mechanotransduction-mediated signaling on cell fate decisions, the ability to recapitulate the adhesive state, cytoskeletal organization, and potentially the tension state of a user-chosen COI presents a new opportunity and approach for investigating adhesion-mediated cellular signaling mechanisms and for producing more homogeneous cell populations. We envision that this approach could potentially be used in a manner somewhat analogous to, and potentially

synergistic with, FACS. Rather than enriching cell populations based on the presence of specific markers, as is done with FACS, one could potentially chose a COI based on immunofluorescent analysis of protein expression or localization and derive a pattern configuration to induce a similar state to the COI. This could drive a chosen cell phenotype through mechanotransduction and also help maintain phenotypes already selected for via FACS. Such a tool could prove extremely useful in investigating the influence of subtle local environmental changes on cell behavior, particularly when moving to high-throughput assay platforms and single-cell analyses.

## MATERIALS AND METHODS

**Cell Culture.** Pooled human umbilical vein endothelial cells were cultured at 37 °C and 5% CO<sub>2</sub> in endothelial growth medium-2 (EGM-2); endothelial basal media-2 (EBM-2) supplemented with an EGM-2 bullet kit (10 mL of fetal bovine serum, 0.2 mL of hydrocortisone, 2 mL of hFGF-B, 0.5 mL of VEGF, 0.5 mL of R3-IGF-1, 0.5 mL of ascorbic acid, 0.5 mL of hEGF, 0.5 mL of gentamicin/amphotericin-B, and 0.5 mL of heparin) in a human plasma fibronectin (Sigma-Aldrich)-coated (3 mL at 10 µg/mL for 30 min at 37 °C) T-25 tissue culture flask; cells and media were from Lonza. Upon 80% confluence, the cells were trypsinized with 3 mL of 0.25% trypsin and 1 mM ethylenediaminetetraacetic acid in PBS at 37 °C for 3 min. The cells were collected and centrifuged for 10 min, the cell pellet was resuspended in 1 mL of EBM-2, and the cell solution was diluted in EGM-2 to the desired concentration. HUVECs were seeded onto patterned surfaces at a density of 40 cells/mm<sup>2</sup>. Passage 3 HUVECs were used for all experiments.

**Metal Deposition.** Circular glass coverslips (35 mm diameter, #1 thickness, optical borosilicate; Fisher Scientific) were cleaned in piranha solution (3:1 H<sub>2</sub>SO<sub>4</sub>/H<sub>2</sub>O<sub>2</sub>) for 1 h, rinsed thoroughly in Millipore water (MPH<sub>2</sub>O) with a resistance of ≥18 MΩ·cm obtained from a Millipore Super-Q water system, and dried with ultra-high-purity nitrogen (N<sub>2</sub>) (Matheson TriGas). Cleaned coverslips were coated with 2 nm titanium followed by 8 nm platinum by evaporating 1/8" × 1/8", 99.999% pure Ti and 1/4" × 1/4", 99.999% pure Pt pellets from 7 cm<sup>3</sup> molybdenum and graphite crucibles, respectively (Kamis Inc.) at rates of 0.5 and 0.1 Å/s, respectively, using an electron-beam evaporator (Sharon Vacuum).

**Virtual Mask Creation.** HUVECs were cultured on FN-coated (1 mL at 10 µg/mL for 30 min at 37 °C) glass coverslips for 16 h, rinsed gently with ice-cold PBS-T (PBS supplemented with 0.01% Tween 20), submerged into ice-cold cytoskeleton stabilizing buffer (CSK: 0.5% Triton X-100, 300 mM sucrose, 10 mM HEPES, 3 mM MgCl<sub>2</sub>, 50 mM NaCl in MPH<sub>2</sub>O, pH 6.8) for 1 min, rinsed with ice-cold CSK, fixed in ice-cold 4% paraformaldehyde in PBS-T for 10 min, and rinsed in PBS-T at 4 °C overnight. The samples were blocked with 10% goat serum in PBS-T for 30 min, rinsed with PBS-T, and incubated with 950 µL of primary antibody solution (2 µg/mL rabbit anti-FN (Abcam) and 2 µg/mL mouse anti-vinculin (Sigma) in 1% goat serum in PBS-T) for 2 h at room temperature. The samples were rinsed thoroughly with PBS-T, incubated with 950 µL of secondary antibody solution (6 µg/mL Alexa Fluor 633 conjugated goat anti-rabbit, 2 µg/mL Alexa Fluor 488 conjugated goat anti-mouse, and 1:20 dilution Alexa Fluor 552 conjugated phalloidin in 1% goat serum in PBS-T, all from Life Technologies) for 1.5 h, rinsed thoroughly with PBS-T, rinsed with MPH<sub>2</sub>O, and gently dried with N<sub>2</sub>. A drop of ProLong Gold Antifade Reagent with DAPI (Life Technologies) was added to the surface and secured with a coverslip.

The samples were imaged on a Zeiss 5LIVE laser scanning confocal microscope (Carl Zeiss) using the appropriate

excitation and emission filters, and specific COIs were chosen. The image of the vinculin containing adhesion sites for each COI was background subtracted using a rolling ball algorithm followed by binarization with an autolocal threshold algorithm using ImageJ (NIH). The cell outline for each COI was traced by hand and binarized using ImageJ. The binarized morphology and adhesion site images for each COI were subdivided into a mosaic of constituent shapes using custom-written MATLAB scripts (MathWorks) based on a published segmentation algorithm.<sup>10,27</sup> Each shape was approximated with a mosaic of quadrilaterals that were used to define regions of interest. Custom-written MATLAB scripts were used to produce an overlay file that could be interpreted by the Zeiss AIM software as a list of these constituent ROIs for each image.<sup>10</sup> Together, the ROIs defined by a given overlay file served as a virtual mask that reconstructed the shape and arrangement of adhesion sites or cell outline for the chosen COI. The composite virtual mask composed of many individual ROIs defined the precise locations for laser-induced thermal patterning.

**Image-Guided Laser Scanning Lithography.** Metalized coverslips were functionalized with a 4 mM ethanolic solution of HS(CH<sub>2</sub>)<sub>11</sub>(OCH<sub>2</sub>CH<sub>2</sub>)<sub>6</sub>OH (OEG) (ProChimia) overnight in a custom-built chamber, rinsed with ethanol, and dried with N<sub>2</sub>.<sup>12</sup> Desired ROIs of the OEG SAM as defined by the virtual mask were thermally desorbed using the "Edit Bleach" software on a Zeiss 5LIVE laser scanning confocal microscope equipped with an automated stage.<sup>11,12</sup> The ROIs were exposed to a 532 nm laser focused through a Zeiss Plan-APOCHROMAT 63× (NA 1.4) oil immersion objective operating at ~8.08 nJ/µm<sup>2</sup> using two passes per ROI in a N<sub>2</sub>-rich environment. The samples were rinsed thoroughly with ethanol, dried with N<sub>2</sub>, exposed to FN (1 mL at 10 µg/mL for 30 min at 37 °C), rinsed thoroughly with PBS, and seeded with HUVECs at a density of 40 cells/mm<sup>2</sup>, and the cells were fixed and immunolabeled for fibronectin, actin, and vinculin, counterstained with DAPI as described in the previous section, and imaged on a Zeiss 5LIVE microscope.

**Image Processing.** The four channel image stack (DAPI, vinculin, actin, fibronectin) for each patterned cell was concatenated into a single four channel stack that also included the images of the COI that the pattern was derived from. All of the images in the stack were aligned using the "AutoAlign Application Module" in Metamorph Software (Molecular Devices LLC). For cells cultured on the morphology-derived pattern configurations, the images of the FN patterns were aligned to the image of the COI's outline that the pattern was derived from, and the images in the three remaining channels were rotated and shifted by the same amount as the aligned FN channel so that all channels were aligned to the same position. Similarly, for cells cultured on the adhesion-derived pattern configurations, the images of the vinculin containing adhesion sites were aligned to the image of the COI's adhesion sites that the pattern was derived from and the remaining three channels were rotated and shifted by the same amount. After alignment, the images were background subtracted and the brightness and contrast autocorrected in

ImageJ. Average images for each channel from images of all of the cells on a chosen pattern configuration were created through an intensity-averaged projection of the single channel stacks using ImageJ. The average intensity projections for each channel were false colored and merged to create average cell images.

**Time-Lapse Confocal Microscopy of GFP-Talin-Transduced HUVECs and Image Analysis.** HUVECs were cultured to 70% confluence in FN-coated T-25 tissue culture flasks and transduced overnight with CellLight talin-GFP, BacMam 2.0 (Life Technologies), a modified baculovirus, at a concentration of 25 particles per cell in EGM-2. After transduction, the EGM-2 containing the virus was aspirated, the cells were rinsed with EGM-2, and phenol-red-free EGM-2 (Lonza) was added to the flask. The transduced HUVECs were trypsinized and seeded onto patterned surfaces at a density of 40 cells/mm<sup>2</sup> in phenol-red-free EGM-2. Four hours postseeding, the HUVECs were imaged at 1 min intervals for 30 min with time-lapse confocal microscopy using the “Time Series” application on a Zeiss 5LIVE confocal microscope in a humidified environmental chamber maintained at 37 °C and 5% CO<sub>2</sub>. The time-lapse images of the talin-GFP were used to track the adhesion sites using “ImarisTrack” in Imaris Software (Bitplane Inc.). The centroid, lifetime, straightness of the adhesion site tracks, number of adhesions present at each time point, and total number of adhesions formed/disassembled over the 30 min duration were measured. The centroid data for each adhesion site were used to determine the mean square displacement, and the random motility coefficient ( $\mu$ ) and persistence time were measured by fitting the mean square displacement data.<sup>28</sup>

**Statistical Analysis.** Statistical analysis was performed using SPSS 12.0 (SPSS). Data set distributions were tested for normality by evaluating the standard error of skewness and kurtosis. The calculated standard errors were between -2 and 2, thereby indicating normally distributed data. Levene's test for the equality of variances was performed to determine if equal variances could be assumed. The significance was greater than 0.1, and therefore equal variances were assumed. One-way ANOVA was implemented with a significance level of 0.05.

**Determination of Cell Architecture and Clustering.** The processed images of the vinculin, actin, and DAPI channels for each cell were used to determine the cell outline using an adaptation of the watershed algorithm. Each channel for every cell was analyzed using a suite of automated image-analysis algorithms written in MATLAB to measure the values for the 40 metrics (see Supplemental Table 1 for a complete description of each metric). A position for each cell was assigned in multidimensional space based on its measured metric values. The members of each cluster were determined using k-means clustering with Euclidian distance as the similarity metric and average linkage. Silhouettes<sup>29</sup> and a stability gap analysis were applied to determine the optimal number of distinct clusters within the multidimensional data set. The two analyses each returned a value of four clusters, which correlated to the number of COIs present in the data set.

**Conflict of Interest:** The authors declare no competing financial interest.

**Acknowledgment.** We are grateful to Z. Iwinski for assistance with software implementation and to W. Deery for assistance with image analysis. This work was supported by grants from the National Institutes of Health (P20EB007076, R01HL097520, R01EB005173, and T32HL007676) and the National Science Foundation (NSF1150645). J.H.S. was supported by postdoctoral fellowships from the National Institutes of Health Nanobiology Training Program of the Keck Center of the Gulf Coast Consortia (T32DK070121) and from the Howard Hughes Medical Institute.

**Supporting Information Available:** A table outlining the details of the metrics used to quantify cytoskeletal architecture, montages of the morphology and adhesion patterns derived from COI 1, the individual channels merged to create the “average” cell images for cells cultured on morphology and adhesion patterns derived from COIs 1 through 4, and

time-lapse GFP-talin images of cells cultured on morphology and adhesion patterns derived from COI 1. The Supporting Information is available free of charge on the ACS Publications website at DOI: 10.1021/acsnano.5b01366.

## REFERENCES AND NOTES

- Lu, X.; Huang, W. H.; Wang, Z. L.; Cheng, H. K. Recent Developments in Single-Cell Analysis. *Anal. Chim. Acta* **2004**, *510*, 127–138.
- Lecault, V.; White, A. K.; Singhal, A.; Hansen, C. L. Microfluidic Single Cell Analysis: From Promise to Practice. *Curr. Opin. Chem. Biol.* **2012**, *16*, 381–390.
- Altschuler, S. J.; Wu, L. F. Cellular Heterogeneity: Do Differences Make a Difference? *Cell* **2010**, *141*, 559–563.
- Wolf, C. R.; Hayward, I. P.; Lawrie, S. S.; Buckton, K.; McIntyre, M. A.; Adams, D. J.; Lewis, A. D.; Scott, A. R. R.; Smyth, J. F. Cellular Heterogeneity and Drug Resistance in Two Ovarian Adenocarcinoma Cell Lines Derived from a Single Patient. *Int. J. Cancer* **1987**, *39*, 695–702.
- Woodruff, M. F. Cellular Heterogeneity in Tumours. *Br. J. Cancer* **1983**, *47*, 589–594.
- Barteneva, N. S.; Ketman, K.; Fasler-Kan, E.; Potashnikova, D.; Vorobjev, I. A. Cell Sorting in Cancer Research—Diminishing Degree of Cell Heterogeneity. *Biochim. Biophys. Acta, Rev. Cancer* **2013**, *1836*, 105–122.
- McBeath, R.; Pirone, D. M.; Nelson, C. M.; Bhadriraju, K.; Chen, C. S. Cell Shape, Cytoskeletal Tension, and Rhoa Regulate Stem Cell Lineage Commitment. *Dev. Cell* **2004**, *6*, 483–495.
- Geiger, B.; Spatz, J. P.; Bershadsky, A. D. Environmental Sensing through Focal Adhesions. *Nat. Rev. Mol. Cell Biol.* **2009**, *10*, 21–33.
- Goffin, J. M.; Pittet, P.; Csucs, G.; Lussi, J. W.; Meister, J. J.; Hinz, B. Focal Adhesion Size Controls Tension-Dependent Recruitment of Alpha-Smooth Muscle Actin to Stress Fibers. *J. Cell Biol.* **2006**, *172*, 259–268.
- Culver, J. C.; Hoffmann, J. C.; Poché, R. A.; Slater, J. H.; West, J. L.; Dickinson, M. E. Three-Dimensional Biomimetic Patterning in Hydrogels to Guide Cellular Organization. *Adv. Mater.* **2012**, *24*, 2344–2348.
- Slater, J. H.; Miller, J. S.; Yu, S. S.; West, J. L. Fabrication of Multifaceted Micropatterned Surfaces with Laser Scanning Lithography. *Adv. Funct. Mater.* **2011**, *21*, 2876–2888.
- Slater, J. H.; West, J. L. Fabrication of Multifaceted, Micro-patterned Surfaces and Image-Guided Patterning Using Laser Scanning Lithography. In *Micropatterning in Cell Biology Part A: Methods in Cell Biology*; Piel, M., Théry, T., Eds.; Elsevier Academic Press, 2014; Vol. 119, pp 193–217.
- Shadnam, M. R.; Kirkwood, S. E.; Fedosejevs, R.; Amirfazli, A. Thermo-Kinetics Study of Laser-Induced Desorption of Self-Assembled Monolayers from Gold: Case of Laser Micropatterning. *J. Phys. Chem. B* **2005**, *109*, 11996–12002.
- Ballestrem, C.; Hinz, B.; Imhof, B. A.; Wehrle-Haller, B. Marching at the Front and Dragging Behind: Differential Alpha-V Beta 3-Integrin Turnover Regulates Focal Adhesion Behavior. *J. Cell Biol.* **2001**, *155*, 1319–1332.
- Hoffman, B. D.; Grashoff, C.; Schwartz, M. A. Dynamic Molecular Processes Mediate Cellular Mechanotransduction. *Nature* **2011**, *475*, 316–323.
- Zaidel-Bar, R.; Itzkovitz, S.; Ma'ayan, A.; Iyengar, R.; Geiger, B. Functional Atlas of the Integrin Adhesome. *Nat. Cell Biol.* **2007**, *9*, 858–868.
- Zamir, E.; Geiger, B.; Kam, Z. Quantitative Multicolor Compositional Imaging Resolves Molecular Domains in Cell-Matrix Adhesions. *PLoS One* **2008**, *3*, 11.
- Zaidel-Bar, R.; Cohen, M.; Addadi, L.; Geiger, B. Hierarchical Assembly of Cell-Matrix Adhesion Complexes. *Biochem. Soc. Trans.* **2004**, *32*, 416–420.
- Geiger, B.; Yamada, K. M. Molecular Architecture and Function of Matrix Adhesions. *Cold Spring Harbor Perspect. Biol.* **2011**, *3*.
- Li, X.; Zhou, Q.; Sunkara, M.; Kutys, M. L.; Wu, Z.; Rychahou, P.; Morris, A. J.; Zhu, H.; Evers, B. M.; Huang, C. Ubiquitylation of Phosphatidylinositol 4-Phosphate 5-Kinase Type II<sup>3</sup>

- by Hectd1 Regulates Focal Adhesion Dynamics and Cell Migration. *J. Cell Sci.* **2013**, *126*, 2617–2628.
- 21. Rosse, C.; Boeckeler, K.; Linch, M.; Radtke, S.; Frith, D.; Barnouin, K.; Morsi, A. S.; Hafezparast, M.; Howell, M.; Parker, P. J. Binding of Dynein Intermediate Chain 2 to Paxillin Controls Focal Adhesion Dynamics and Migration. *J. Cell Sci.* **2012**, *125*, 3733–3738.
  - 22. Chan, K. T.; Bennin, D. A.; Huttenlocher, A. Regulation of Adhesion Dynamics by Calpain-Mediated Proteolysis of Focal Adhesion Kinase (Fak). *J. Biol. Chem.* **2010**, *285*, 11418–11426.
  - 23. Franco, S. J.; Rodgers, M. A.; Perrin, B. J.; Han, J. W.; Bennin, D. A.; Critchley, D. R.; Huttenlocher, A. Calpain-Mediated Proteolysis of Talin Regulates Adhesion Dynamics. *Nat. Cell Biol.* **2004**, *6*, 977–983.
  - 24. Pelham, R. J.; Wang, Y. L. Cell Locomotion and Focal Adhesions Are Regulated by Substrate Flexibility. *Proc. Natl. Acad. Sci. U.S.A.* **1997**, *94*, 13661–13665.
  - 25. Kilian, K. A.; Bugarija, B.; Lahn, B. T.; Mrksich, M. Geometric Cues for Directing the Differentiation of Mesenchymal Stem Cells. *Proc. Natl. Acad. Sci. U.S.A.* **2010**, *107*, 4872–4877.
  - 26. Singhvi, R.; Kumar, A.; Lopez, G. P.; Stephanopoulos, G. N.; Wang, D. I. C.; Whitesides, G. M.; Ingber, D. E. Engineering Cell-Shape and Function. *Science* **1994**, *264*, 696–698.
  - 27. Geraets, W. G. M.; van Daatselaar, A. N.; Verheij, J. G. C. An Efficient Filling Algorithm for Counting Regions. *Comput. Meth. Programs Biomed.* **2004**, *76*, 1–11.
  - 28. Dickinson, R. B.; Tranquillo, R. T. Optimal Estimation of Cell-Movement Indexes from the Statistical-Analysis of Cell Tracking Data. *AIChE J.* **1993**, *39*, 1995–2010.
  - 29. Rousseeuw, P. J. Silhouettes: A Graphical Aid to the Interpretation and Validation of Cluster Analysis. *J. Comput. Appl. Math.* **1987**, *20*, 53–65.

# Supporting Information for

## Recapitulation and Modulation of the Cellular Architecture of a User-Chosen Cell of Interest Using Cell-Derived, Biomimetic Patterning

*John H. Slater, James C. Culver, Byron L. Long, Chenyue W. Hu, Jingzhe Hu, Taylor F. Birk, Amina A. Qutub,  
Mary E. Dickinson, and Jennifer L. West*

**Supplemental Table 1:** Metrics Used to Define Cellular Architecture

<b>Cell Metrics</b>		
<b>Metric</b>	<b>Description</b>	<b>Mathematical Representation</b>
<b>Morphology Metrics</b>		
Cell Size	Cell spread area.	$A_C$
Circularity	Shape factor.	$\frac{4\pi \cdot A_C}{P_C^2}$ , where $P_c$ = Cell Perimeter
Elongation	Shape factor.	$\frac{P_C}{A_C}$
<b>Adhesion Site Metrics</b>		
Number of Adhesion Sites	Number of adhesions per cell.	$N_A$
Adhesion Total Area	Sum of the area of all adhesions.	$\sum N_A$
Polarity	Distance between the center of mass of the vinculin stain and the centroid of the cell.	$\sqrt{(\chi_{C,x} - \Omega_{V,x})^2 + (\chi_{C,y} - \Omega_{V,y})^2}$ , where $\chi_C$ = centroid of the cell $C$ $\Omega_V$ = center of mass of the vinculin stain $V$
Maximum Intensity	The maximum of the average vinculin stain intensities of all 10 bands*	$\max(\{I_{B_1} \dots I_{B_{10}}\})$
Maximum Location	The index of the band* with the highest average vinculin stain intensity	The least $n$ such that $I_{B_n} = \max(\{I_{B_1} \dots I_{B_{10}}\})$

Above Average Adjusted Distribution	Adjusted, weighted sum of average vinculin stain intensities greater than the mean intensity.	$\frac{\sum_{k=1}^{10} s(I_{B_k}) \cdot I_{B_k} \cdot k}{\max(\{I_{B_1} \dots I_{B_{10}}\}) \cdot \sum_{k=1}^{10} s(I_{B_k})}$
Slope	Slope of average vinculin stain intensity between bands* $B_8$ and $B_2$ .	$\frac{I_{B_8} - I_{B_2}}{8 - 2}$
Comparison to COI	The sum of the Euclidean distance between nearest neighbors of the COI (cell-of-interest) and a second cell (patterned cell) using the COI adhesion sites as reference plus the patterned cells as reference; the shorter the distance, the closer the match; COI compared to COI is an exact match.	$\sum_{NN=1}^{N_A} \sqrt{(\chi_{A,COI,x}^{NN} - \chi_{A,C,x}^{NN})^2 + (\chi_{A,COI,y}^{NN} - \chi_{A,C,y}^{NN})^2}$ using both for the COI and the patterned cell as the initial cell of reference $NN = \text{nearest neighbor adhesion site}$ $\chi_A = \text{centroid of the adhesion site A}$

### Actin Cytoskeleton Metrics

Polarity	Distance between the center of mass of actin and the centroid of the cell.	$\sqrt{(\chi_{C,x} - \Omega_{A,x})^2 + (\chi_{C,y} - \Omega_{A,y})^2}$ where $\Omega_A = \text{center of mass of actin}$
Uniformity	Sum of squared elements in the histogram counts of the image for pixel intensities. Analogous to energy or sum of squared elements in the grayscale co-occurrence matrix.	$\sum p^2$
Entropy From Histogram	Measure of randomness of the image where $p$ is the histogram counts of the image for pixel intensities, with 256 possible bins for a grayscale image.	$-\sum p * \log_2(p)$
Entropy From GLCM	Measure of randomness of the image where $g$ is the histogram counts of the gray level co-occurrence matrix of the image.	$-\sum g * \log_2(g)$
Correlation	A measure of Pearson's correlation of each pixel to its neighborhood over the whole image. For a perfectly linearly and positively correlated set of pixels, correlation = 1.	$\sum_{i,j} \frac{(i - \mu_i)(j - \mu_j)p(i, j)}{\sigma_i \sigma_j}$
Energy	Sum of squared elements in the grayscale co-occurrence matrix.	$\sum_{i,j} p(i, j)^2$
Homogeneity	Measure of the closeness of the distribution of elements in the grayscale co-occurrence matrix to the diagonal of the matrix. For a diagonal matrix, homogeneity = 1.	$\sum_{i,j} \frac{p(i, j)}{1 +  i - j }$
Maximum Location	The index of the band* with the highest average actin stain intensity	Similar to Adhesion Site maximum location
Above Average Adjusted Distribution	Weighted average location (as a band* index) of the actin stain bands	Similar to Adhesion Site mean location above average

with intensity greater than the mean intensity.

Fiber Alignment Match	Sum of squares difference between histograms of COI and pattern cell actin fiber orientation	$\sum_{i=1}^N (h_{COI,i} - h_{pattern,i})^2$
		$N =$ number of histogram bins $h_i =$ size of $i$ -th bin of histogram

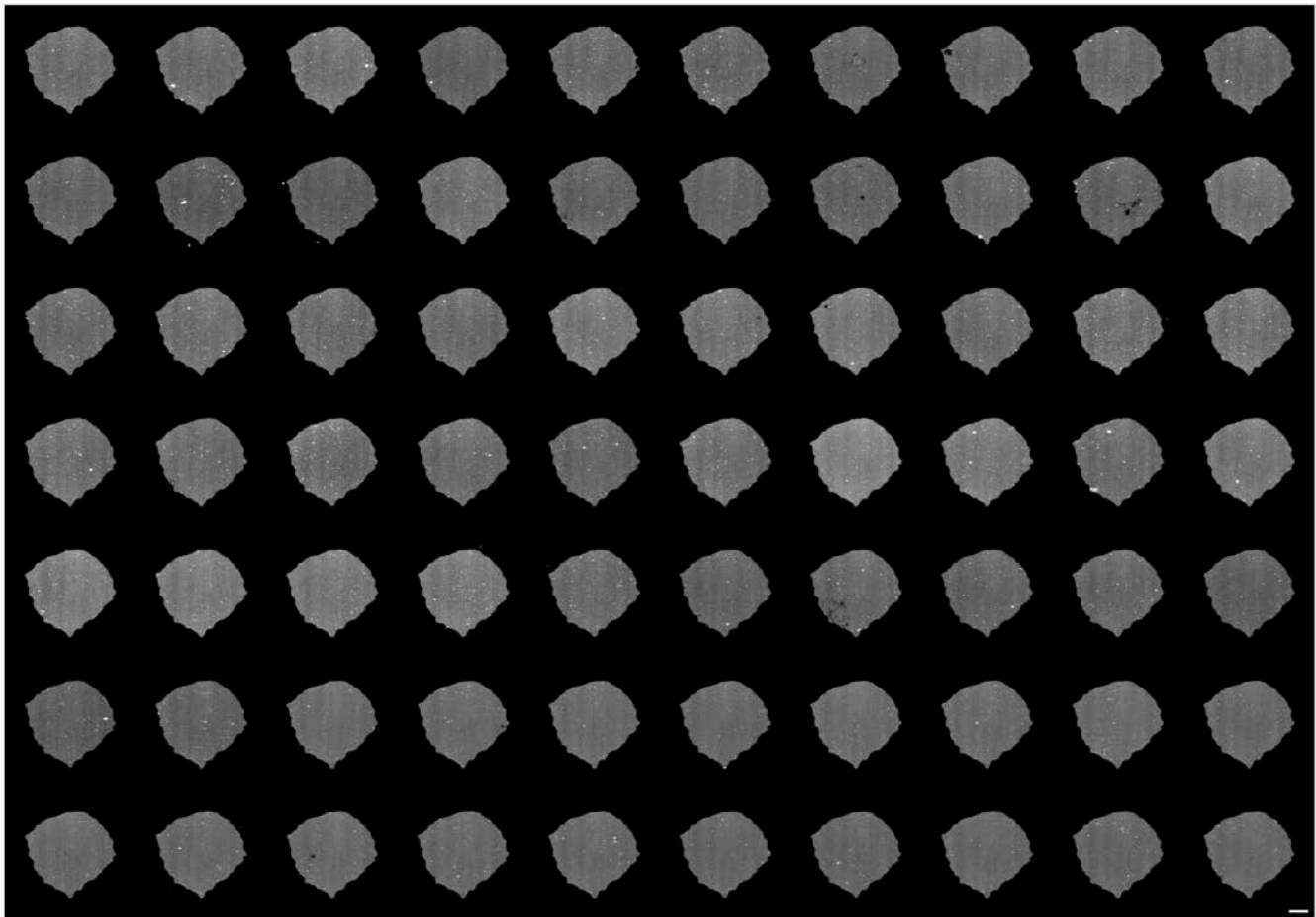
### Nucleus Metrics

---

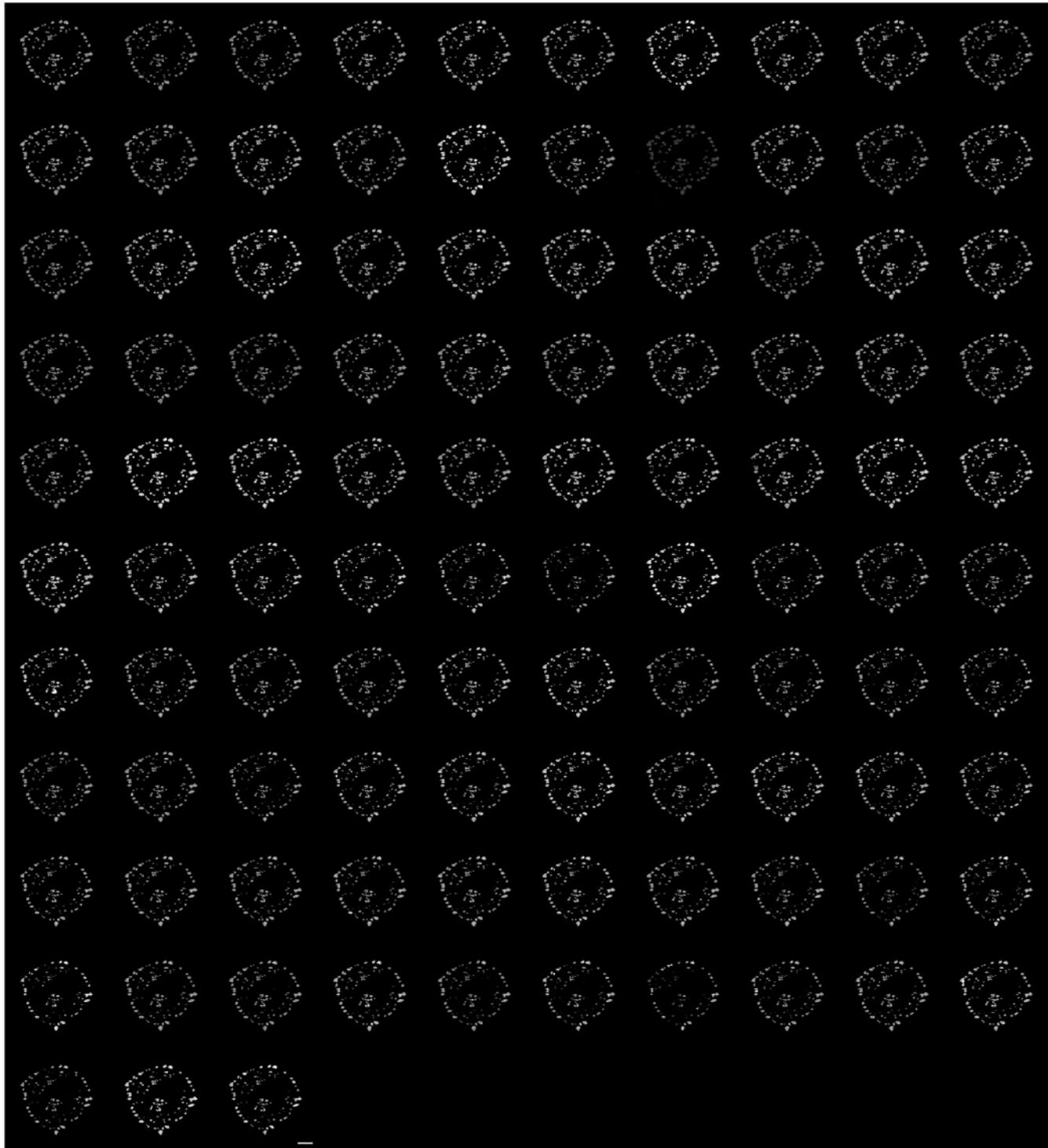
Major Axis Length	Length of major axis.	$l_{N, Major}$
Minor Axis Length	Length of minor axis.	$l_{N, Minor}$
Major Minor Axis Ratio	Axis length ratio	$\frac{l_{N, Major}}{l_{N, Minor}}$
Polarity	Distance between the center of mass of DAPI and the centroid of the cell.	$\sqrt{(\chi_{C,x} - \Omega_{D,x})^2 + (\chi_{C,y} - \Omega_{D,y})^2}$ where $\Omega_D$ = center of mass of DAPI

---

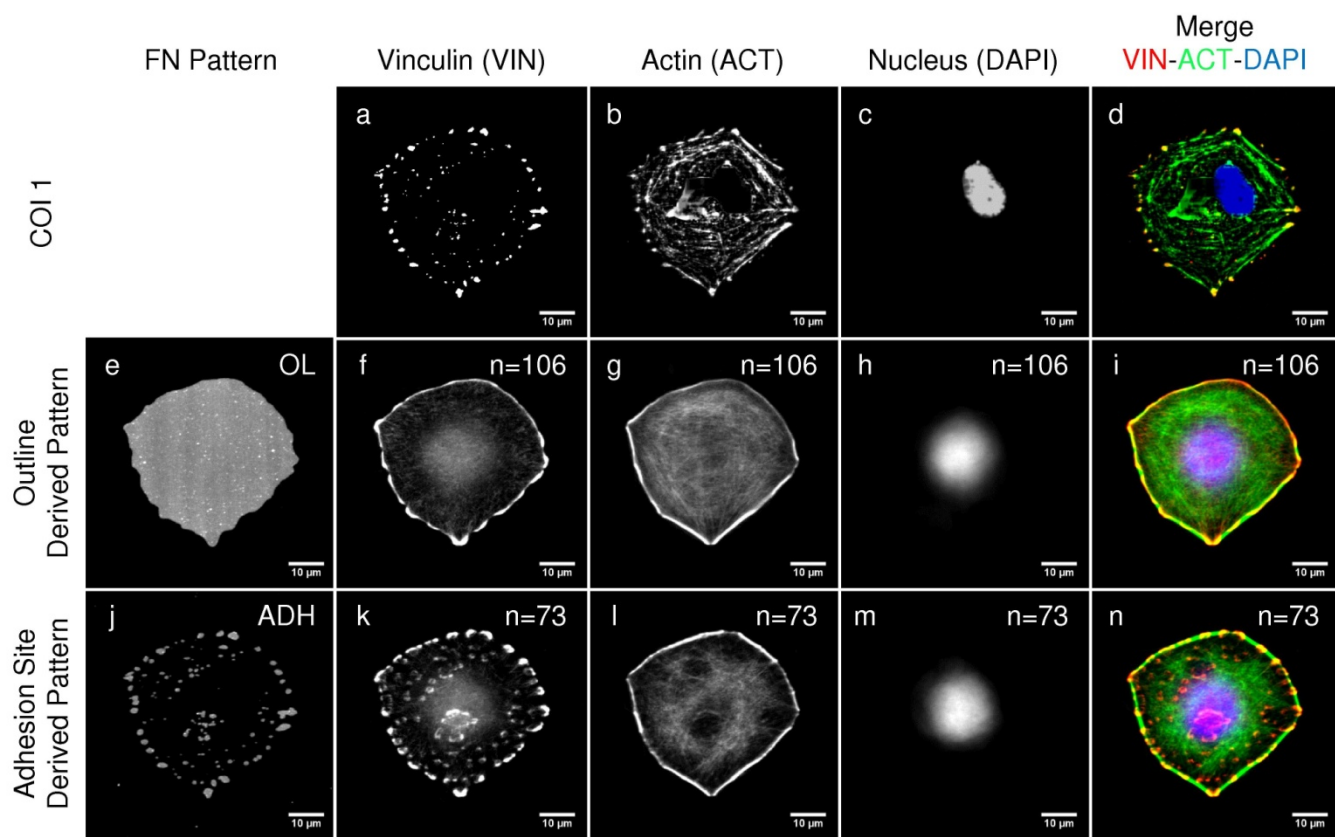
\* A band is a locus of points within the cell cytoplasm at a relative distance from the nucleus. Let  $r$  range over segments of lines radiating from the centroid of a cell nucleus starting at the nucleus perimeter and ending at the cell perimeter. Let  $r_n$  ( $1 \leq n \leq 10$ ) denote the  $n$ -th of 10 equi-length, separate, and consecutive subsegments of  $r$ . For a given cell, band  $B_n$  ( $1 \leq n \leq 10$ ) is the locus of all  $r_n$ .



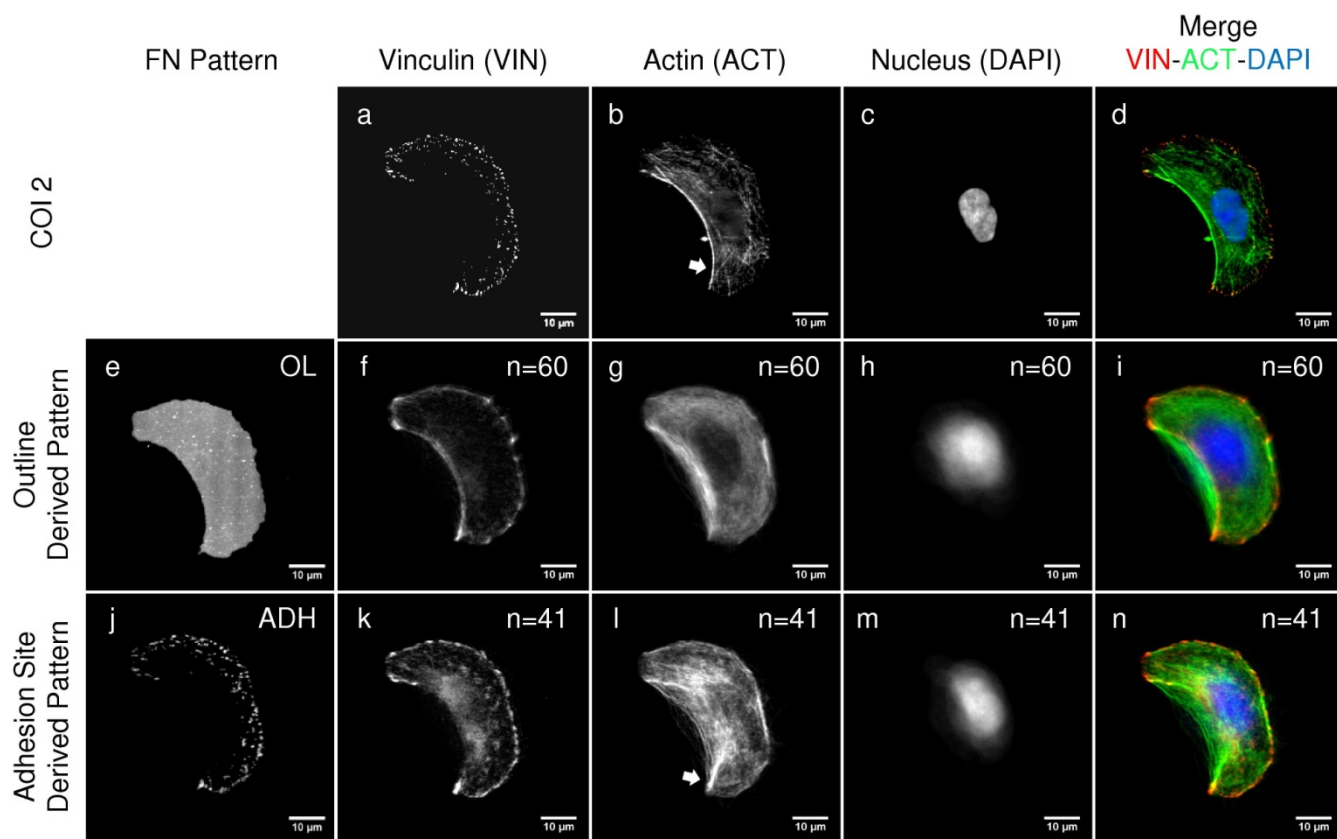
**Supplemental Figure 1:** Montage of images of the morphology pattern derived from COI 1. An outline of COI 1 was used to define this fibronectin pattern configuration. Arrays of the FN pattern were created with IG-LSL, fluorescently immunolabeled, imaged, and compiled into a montage. SB=10  $\mu$ m.



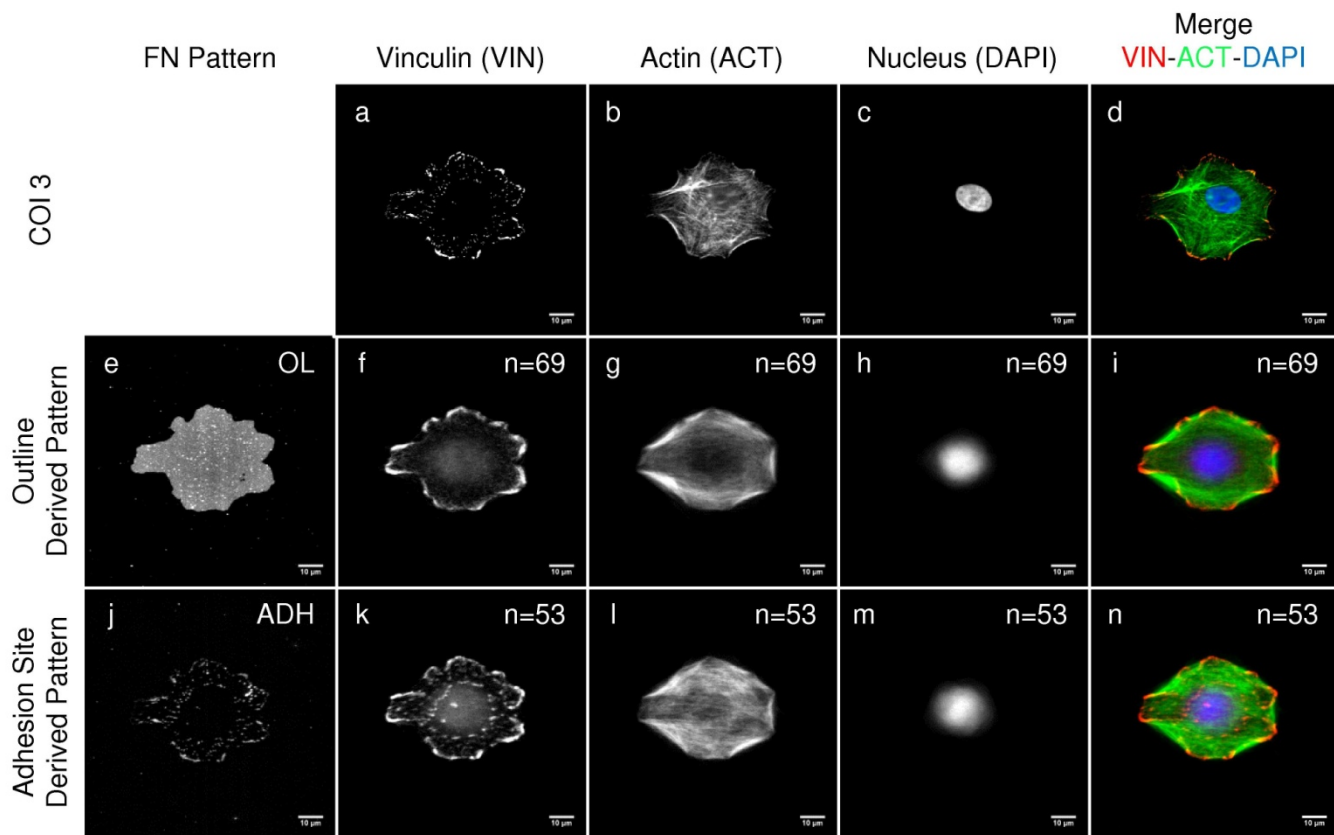
**Supplemental Figure 2:** Montage of images of the adhesion pattern derived From COI 1. An image of the vinculin-containing adhesion sites of COI 1 was used to define this fibronectin pattern configuration. Arrays of the FN pattern were created with IG-LSL, fluorescently immunolabeled, imaged, and compiled into a montage. SB=10  $\mu$ m.



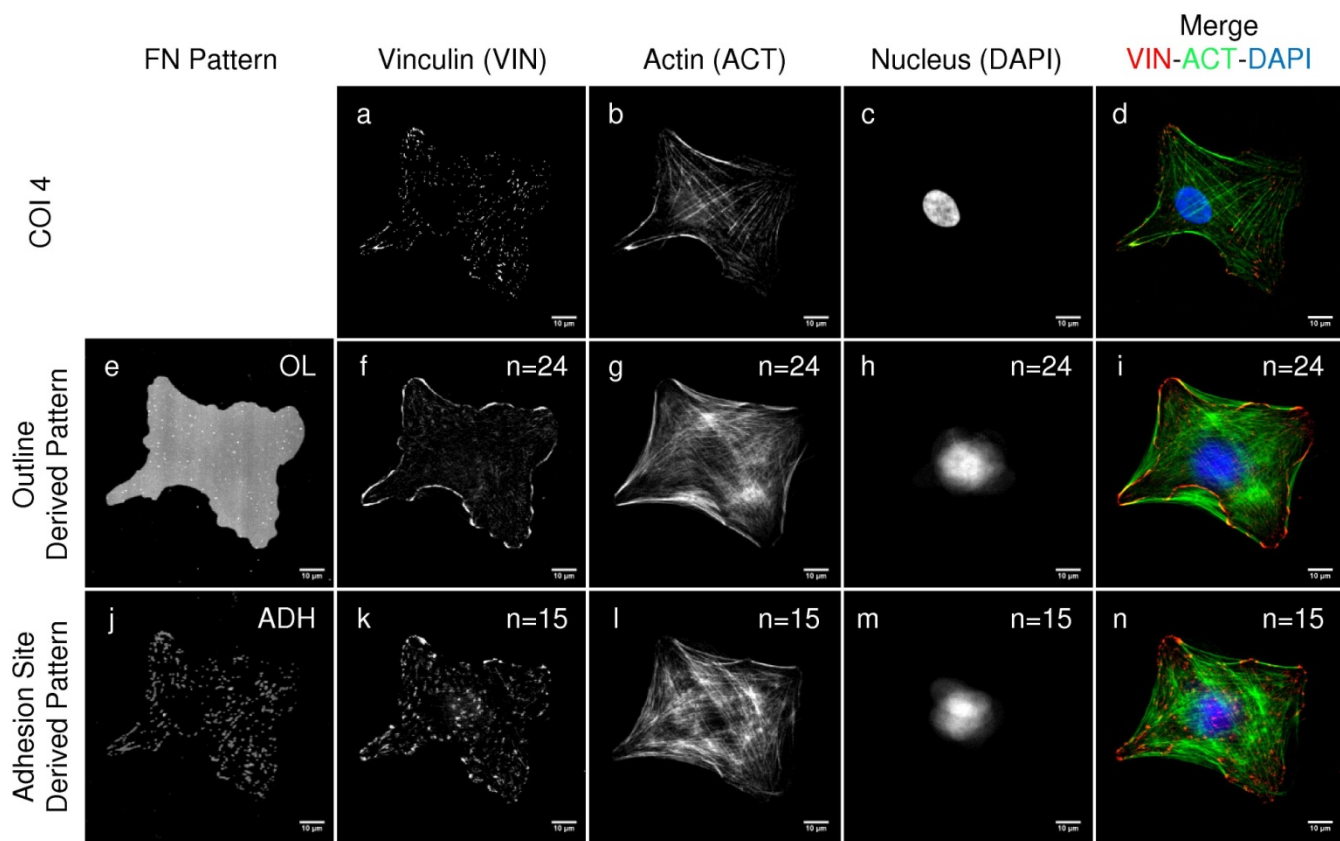
**Supplemental Figure 3:** ‘Average’ cells cultured on patterns derived from COI 1. (a-d) Fluorescent images of the vinculin-containing adhesions, actin cytoskeleton, and nucleus of COI 1 that the (e,j) FN pattern configurations were derived from. HUVECs were cultured on arrays of the (e) morphology (OL) or (j) adhesion site (ADH) derived pattern configuration, fixed, fluorescently immunolabeled for vinculin, actin, counterstained with DAPI, and imaged. (f-h, k-m) The individual cell images, n = 106 and 73 for the number of cells cultured on the (f-h) morphology and (k-m) adhesion site derived pattern configurations respectively, for each channel were aligned, overlaid, and intensity averaged. SB=10 μm.



**Supplemental Figure 4:** ‘Average’ cells cultured on patterns derived from COI 2. (a-d) Fluorescent images of the vinculin-containing adhesions, actin cytoskeleton, and nucleus of COI 2 that the (e,j) FN pattern configurations were derived from. HUVECs were cultured on arrays of the (e) morphology (OL) or (j) adhesion site (ADH) derived pattern configuration, fixed, fluorescently immunolabeled for vinculin, actin, counterstained with DAPI, and imaged. (f-h, k-m) The individual cell images,  $n = 60$  and  $41$  for the number of cells cultured on the (f-h) morphology and (k-m) adhesion site derived pattern configurations respectively, for each channel were aligned, overlaid, and intensity averaged. SB=10  $\mu\text{m}$ .



**Supplemental Figure 5:** ‘Average’ cells cultured on patterns derived from COI 3. (a-d) Fluorescent images of the vinculin-containing adhesions, actin cytoskeleton, and nucleus of COI 3 that the (e,j) FN pattern configurations were derived from. HUVECs were cultured on arrays of the (e) morphology (OL) or (j) adhesion site (ADH) derived pattern configuration, fixed, fluorescently immunolabeled for vinculin, actin, counterstained with DAPI, and imaged. (f-h, k-m) The individual cell images,  $n = 69$  and  $53$  for the number of cells cultured on the (F-H) morphology and (k-m) adhesion site derived pattern configurations respectively, for each channel were aligned, overlaid, and intensity averaged. SB=10  $\mu\text{m}$ .



**Supplemental Figure 6:** ‘Average’ cells cultured on patterns derived from COI 4. (a-d) Fluorescent images of the vinculin-containing adhesions, actin cytoskeleton, and nucleus of COI 4 that the (e, j) FN pattern configurations were derived from. HUVECs were cultured on arrays of the (e) morphology (OL) or (j) adhesion site (ADH) derived pattern configuration, fixed, fluorescently immunolabeled for vinculin, actin, counterstained with DAPI, and imaged. (f-h, k-m) The individual cell images, n = 24 and 15 for the number of cells cultured on the (f-h) morphology and (k-m) adhesion site derived pattern configurations respectively, for each channel were aligned, overlaid, and intensity averaged. SB=10 μm.